Kinetic and perfusion modeling of hyperpolarized ^{13}C pyruvate and urea in cancer with arbitrary RF flip angles

Naeim Bahrami, Christine Leon Swisher, Cornelius Von Morze, Daniel B. Vigneron, Peder E. Z. Larson

Department of Radiology and Biomedical Imaging, University of California – San Francisco, San Francisco, CA, USA
Corresponding to: Naeim Bahrami. Department of Radiology and Biomedical Imaging, University of California, San Francisco, USA. Email: naeim.bahrami@gmail.com.

Abstract: The accurate detection and characterization of cancerous tissue is still a major problem for the clinical management of individual cancer patients and for monitoring their response to therapy. MRI with hyperpolarized agents is a promising technique for cancer characterization because it can non-invasively provide a local assessment of the tissue metabolic profile. In this work, we measured the kinetics of hyperpolarized [1-^{13}C] pyruvate and ^{13}C-urea in prostate and liver tumor models using a compressed sensing dynamic MRSI method. A kinetic model fitting method was developed that incorporated arbitrary RF flip angle excitation and measured a pyruvate to lactate conversion rate, Kpl, of 0.050 and 0.052 (1/s) in prostate and liver tumors, respectively, which was significantly higher than Kpl in healthy tissues [Kpl =0.028 (1/s), P<0.001]. Kpl was highly correlated to the total lactate to total pyruvate signal ratio (correlation coefficient =0.95). We additionally characterized the total pyruvate and urea perfusion, as in cancerous tissue there is both existing vasculature and neovascularization as different kinds of lesions surpass the normal blood supply, including small circulation disturbance in some of the abnormal vessels. A significantly higher perfusion of pyruvate (accounting for conversion to lactate and alanine) relative to urea perfusion was seen in cancerous tissues (liver cancer and prostate cancer) compared to healthy tissues (P<0.001), presumably due to high pyruvate uptake in tumors.

Keywords: Hyperpolarized carbon-13; metabolic imaging; cancer; perfusion; kinetic modeling; dynamic MRSI

Introduction

Hyperpolarization is the nuclear spin polarization of a material far beyond thermal equilibrium conditions. The accurate and correct diagnosis and characterization of cancer is still a major problem for the clinical management of every kind of cancer patients, including individual prostate or liver cancer patients, and also in order to monitor their response to therapy (1-3). Magnetic resonance spectroscopic imaging (MRSI) with hyperpolarized ^{13}C labeled substrates is a new method to study any cancers that may be able to simultaneously and noninvasively assess changes in metabolic intermediates from multiple biochemical pathways of interest.

Recent studies have shown a large amount of potential applications of hyperpolarized (HP) ^{13}C MRSI for the *in vivo* monitoring of cellular metabolism and the characterization of disease. The low natural abundance and sensitivity of ^{13}C compared to protons poses a technical challenge using conventional approaches (4,5). Dynamic nuclear polarization (DNP) of ^{13}C labeled pyruvate and subsequent rapid dissolution generates a contrast agent with a four order-of-magnitude sensitivity enhancement that is injected and gives the ability to monitor the spatial distribution of pyruvate and its conversion to lactate, alanine, and bicarbonate. The conversion of pyruvate to lactate catalyzed by the enzyme lactate dehydrogenase is of particular interest, as the kinetics of this process have been shown to be sensitive to the presence and severity of disease in preclinical models (6,7).

HP MRSI can also be used to measure perfusion that in cancer can reflect spatially heterogeneous changes to existing vasculature and neovascularization as tumors

surpass the normal blood supply, including microcirculatory disturbance in abnormal vessels. Tumor perfusion data in addition to the metabolic data available from spectroscopic imaging of ^{13}C pyruvate would be of important value in exploring the complex relationship between perfusion and metabolism in cancer at both preclinical and clinical research levels (8-11).

The primary purpose of this research was to study the dynamics of simultaneously injected HP [1-^{13}C]-pyruvate and ^{13}C-urea to provide improved characterization of cancerous tissues. To achieve rapid, 2 s temporal resolution, whole mouse MRSI we used a 18-fold accelerated compressed sensing acquisition and reconstruction with smaller flip angles for pyruvate and urea compared to lactate and alanine for efficient usage of the hyperpolarized magnetization by preserving the substrate. This flip angle scheme required using a modified kinetic model that accounts for arbitrary RF flip angles (12-15). Data was acquired in mice with prostate and liver cancer and comparisons were made to normal tissues such as kidney and healthy liver of the metabolite concentrations, including Urea, Pyruvate, and Lactate, the conversion constant (Kpl) between pyruvate to lactate, and the conversion constant (Kpa) between pyruvate to alanine. We also created novel parameterizations of the total pyruvate and urea perfusions in order to assess vascular delivery and tissue uptake. A key new feature of our modeling is the ability to detect metabolic conversion, magnetization exchange between compounds, and perfusion when using arbitrary RF flip angles for different compounds.

Methods

Kinetic modeling with variable flip angles

The kinetics of the HP pyruvate magnetization can be modeled as:

$$\frac{d}{dt}\begin{bmatrix} Mp(t) \\ Ml(t) \\ Ma(t) \end{bmatrix} = \begin{bmatrix} -\rho_p - Kpl - Kpa & 0 & 0 \\ Kpl & \rho_l & 0 \\ Kpa & 0 & \rho_a \end{bmatrix}\begin{bmatrix} Mp(t) \\ Ml(t) \\ Ma(t) \end{bmatrix} \quad [1]$$

where ρ_p, ρ_l, and ρ_a, are the longitudinal magnetization relaxation rates for pyruvate, lactate and alanine, respectively, Kpl is the conversion rate from pyruvate to lactate, and Kpa is the conversion rate from pyruvate to alanine. We assumed the reverse conversion rates were negligible.

Eq. [2a-d] show the solution to this kinetic model as well as for urea of the longitudinal magnetization:

$$Mzu(t) = Cu. e^{-(\rho_u)t} \quad [2a]$$

$$Mzp(t) = Cp. e^{-(Kpl+Kpa+\rho_p)t} \quad [2b]$$

$$Mzl(t) = \frac{Cp.Kpl}{\rho_l - Kpl - Kpa - \rho_p}. e^{-(Kpl+Kpa+\rho_p)t} + Cl. e^{-\rho_l t} \quad [2c]$$

$$Mza(t) = \frac{Cp.Kpa}{\rho_a - Kpl - Kpa - \rho_p}. e^{-(Kpl+Kpa+\rho_p)t} + Ca. e^{-\rho_a t} \quad [2d]$$

As it can be observed the lactate and alanine magnetization will decay based on their relaxation rate while there is some addition because of metabolic conversion from pyruvate.

The flip angle effects on the longitudinal magnetization when acquiring an image can be described in the following equation for the change in MZ:

$$\Delta M_{zx}[n] = \frac{S_x[n] - (M_{zx}[n-1].\sum_{k=1}^{N}\sin\theta_x.(\cos\theta_x)^{k-1})}{\sin\theta_x} \quad [3]$$

where x represents pyruvate, lactate, alanine, or urea, θ_x is the appropriate flip angle for the metabolite (12 degrees for lactate and alanine and six degrees for pyruvate and urea in our experiments), N is the number of flip angles per image (N=8 in our data), and the signal S_x.

We used a discretized model in which first the change in longitudinal magnetization due to the RF pulses (Eq. 3) was calculated for each time point (assuming N instantaneous excitations), and then was followed by a period of magnetization evolution as in Eq. [2a-d]. This was repeated for each time point acquired.

In simulations we found that obtaining a good fit with our SNR required assuming that the relaxation rates, ρ_l, of pyruvate, lactate, and alanine were identical.

Ratio of metabolites model

We also speculated that the ratio of total lactate signal to total pyruvate signal would be commensurate with Kpl. In other words, with summing all time points and assuming a constant ratio, we speculate:

$$\frac{\sum_{i=1}^{Nt} Li}{\sum_{i=1}^{Nt} Pi} = C * Kpl \quad [4]$$

where Nt is number of time points, Li and Pi are lactate and pyruvate peak values, respectively. This relationship is strictly true across different voxels provided we assume a constant lactate relaxation rate and identical delivery time of pyruvate.

Perfusion parameterization

Our studies included HP ^{13}C-urea as an independent marker of perfusion. To quantify this perfusion, we propose perfusion parameters of urea perfusion as well as total

26

Bahrami et al. Hyperpolarized ^{13}C kinetic and perfusion modeling

pyruvate perfusion, which accounts for pyruvate signal losses due to conversion to lactate and alanine. For total pyruvate perfusion, we propose:

$$P_p = \int_0^\infty \hat{M}_{zP}(t) + \hat{M}_{zL}(t) + \hat{M}_{zA}(t) \, dt \qquad [5]$$

Where P_p is pyruvate perfusion accumulation and $\hat{M}$ is the longitudinal magnetization of pyruvate, lactate, and alanine as calculated by the kinetic model (i.e., based on the fitted relaxation and conversion rates, without the influence of RF pulses). For the urea perfusion we propose:

$$P_u = \int_0^\infty \hat{M}_{zU}(t) dt \qquad [6]$$

Where P_u is the urea perfusion and $\hat{M}$ is the longitudinal magnetization of urea as calculated by the model. For an initial magnetization $M_{zU}(0)$ we have:

$$P_u = \int_0^\infty M_{zU}[0].e^{-t\rho_u} dt = M_{zU}[0]/\rho_u \qquad [7]$$

When we are assuming that ρ_l, ρ_a, and ρ_p are equal, we can derive the accumulation of pyruvate perfusion as:

$$P_p = \int_0^\infty (M_{zP}[0] + M_{zL}[0] + M_{zA}[0]).e^{-t\rho_p} dt$$
$$= (M_{zP}[0] + M_{zL}[0] + M_{zA}[0])/\rho_p \qquad [8]$$

If ρ_l, ρ_a, and ρ_p are not equal, the full expressions from Eq. [2b-d] can be used.

In vivo studies

The transgenic adenocarcinoma of mouse prostate (TRAMP) murine model is a well-characterized model of prostate cancer that mimics the rapid disease progression, histopathology and metabolic changes observed in human disease. These mice are widely used in the identification of novel biomarkers and molecular mechanisms associated with disease progression, as well as in the investigation of new strategies for characterizing and treating human prostate cancers. We used these mice as a model system of human prostate cancer to test the proposed kinetic and perfusion methods. We also used a Tet-o-MYC/LAP-tTA double transgenic mouse model of liver cancer, in which the MYC oncogene can be inactivated by including doxycycline (doxy) in the mouse diet, allowing for switching on and off oncogene expression (16,17).

We studied n=4 TRAMP and n=3 MYC-driven liver cancer mice when they had developed solid tumors (>0.5 cc)

clearly visible in 1H MRI. All animal studies were carried out under a protocol approved by our Institutional Animal Care and Use Committee. Experiments were performed on a GE 3 T clinical MRI system (GE Healthcare, Waukesha, WI, USA) with 40 mT/m, 150 mT/m/ms gradients and a broadband RF amplifier. A custom built, dual-tuned mouse birdcage coil was used for RF transmission and signal reception. [1-^{13}C] pyruvate and ^{13}C-urea mixtures with a trityl radical were simultaneously polarized in a HyperSense DNP system (Oxford Instruments, Abingdon, UK) at 3.35 T and a temperature of 1.3 K. 350 μL of a dissolved 80 mM (pyruvate) and 115 mM (urea) solution was injected into the tail vein over 12 seconds.

We used a 3D hyperpolarized ^{13}C dynamic MRSI acquisition with multiband excitation pulses and a compressed sensing acquisition and reconstruction. The multiband excitation pulse was modified to include an excitation band for ^{13}C-urea, with flip angles of 6-degrees for [1-^{13}C]-pyruvate and ^{13}C-urea, and 12-degrees for [1-^{13}C]-lactate and [1-^{13}C]-alanine. The acquisition was started after completion of the injection and minimal spin-echo crusher gradient amplitudes were used to minimize saturation of flowing ^{13}C-labelled molecules. Other sequence parameters included an adiabatic double spin-echo with TE =155 ms, TR =250 ms, 10 Hz spectral resolution, 581 Hz spectra bandwidth, 12×12×16 matrix, 5 mm × 5 mm × 5.4 mm resolution, and 2 s per image.

Results

On seven mice, HP ^{13}C MRSI and the anatomical imaging were performed. *Figure 1A,B* present anatomical MR datasets from the prostate and kidney for one of the animals with prostate cancer. HP ^{13}C pyruvate is detectable in each voxel in the body. The signal from a prostate cancer voxel and the fit signal are shown on *Figure 1C,D*, respectively, and noisy, approximately exponential decay can be observed.

Mapping of the Kpl and lactate to pyruvate signal ratio in different slices of cancerous tissue and healthy tissue is presented in *Figures 2,3*. As expected, the HP ^{13}C lactate signal and Kpl was much higher in the tumor regions. The maps also qualitatively show a good correspondence between Kpl and lactate to pyruvate ratio.

Table 1 illustrates the average metabolites' ρ_1 values, Kpl, and Kpa in the prostate and liver tumor tissues, respectively, extracted by our fitting method. According to the literature, *in vivo* T$_1$ values of HP ^{13}C urea and pyruvate are in range of 30-40 s, respectively (18-20). Likewise, T$_1$ values reported
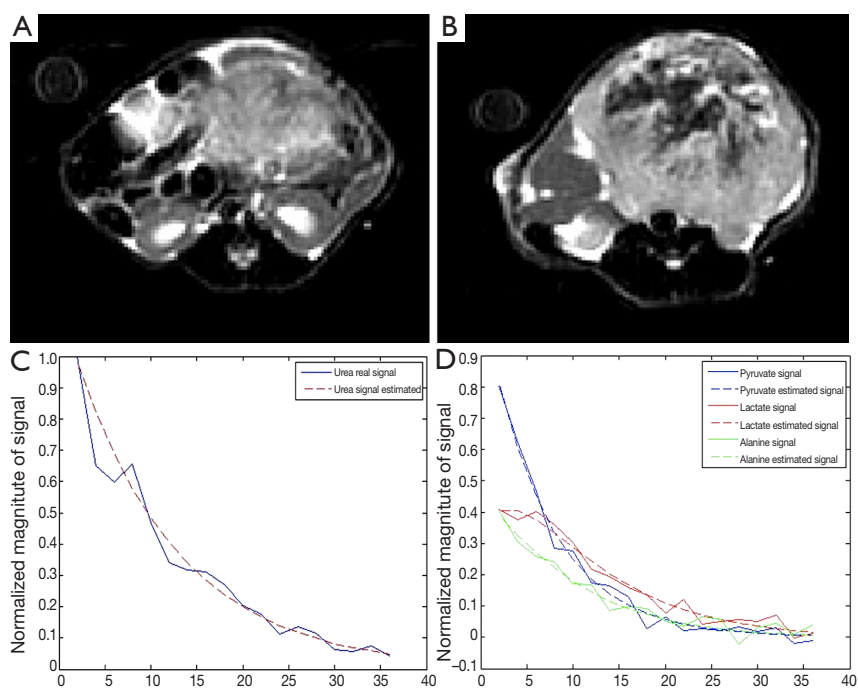
Figure 1 The image in the top left (A) shows a slice which is including the kidneys and the top right (B) one shows the prostate cancerous tissue in a TRAMP mouse. Real (solid) and fit (dashed) signal curves in a prostate tumor voxel for urea (C) and pyruvate, lactate, and alanine (D).
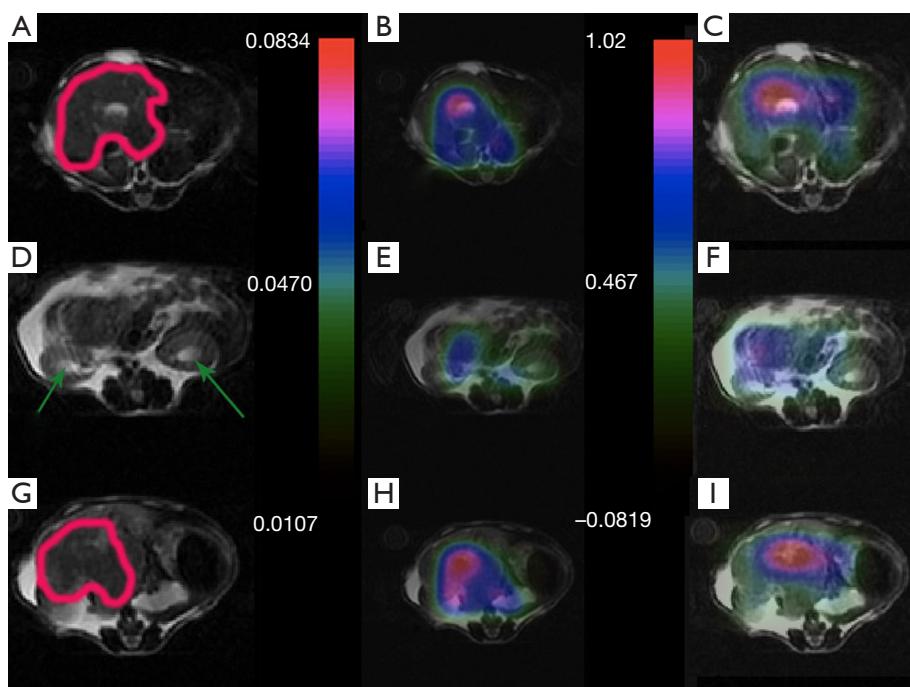

Figure 2 Mapping of the Kpl and lactate to pyruvate signal ratio in liver cancer. Anatomical images of liver cancer (red boundary), kidneys (arrows), and liver including both cancerous and healthy voxels are shown in (A), (B), and (C), respectively. The corresponding Kpl maps in (D-F) and lactate to pyruvate signal ratio (G-I) are elevated in the tumor regions and show good agreement between these different metabolism parameterizations.
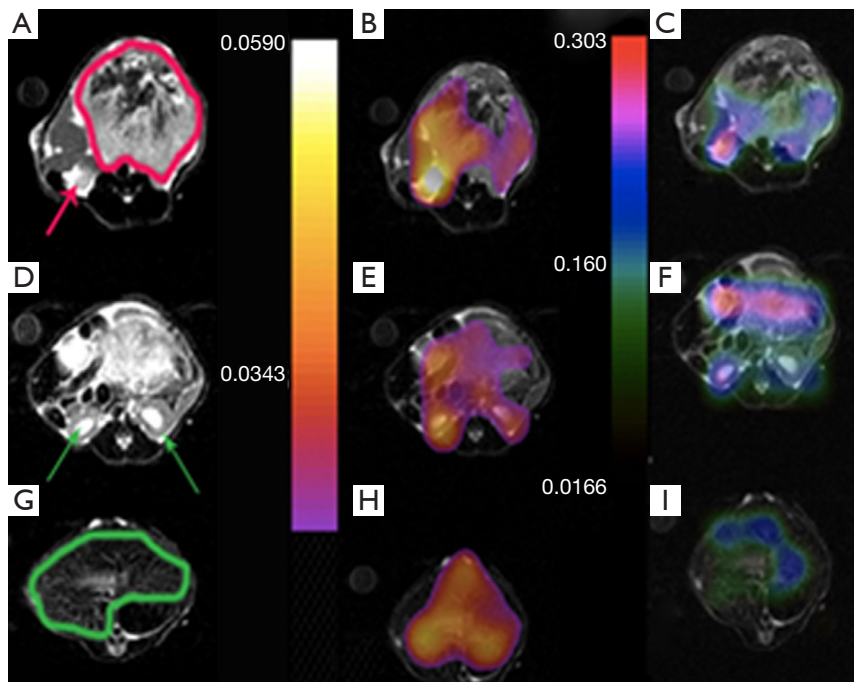
Figure 3 Mapping of the Kpl and lactate to pyruvate signal ratio in prostate cancer. Anatomical images of prostate cancer (red boundary) and a metastasis (red arrow), kidney (green arrows), and healthy liver (green boundary) slices are shown in (A), (B) and (C), respectively. The corresponding Kpl maps (D-F) and lactate to pyruvate signal ratio (G-I) are elevated in the tumor and the metastases. The tumor can be seen in the central slice anterior to the kidneys.

Table 1 Average ρ_l values and conversion constant rates in kidney, healthy and cancerous liver, and prostate tumor for the animals with prostate cancer

	ρ_l of urea (s^{-1})	ρ_l of pyruvate and its products (s^{-1})
Kidney	0.130	0.090
Healthy liver	0.075	0.061
Cancerous liver	0.130	0.077
Prostate tumor	0.150	0.083

Figure 4 Kpl values (mean and standard deviation) in four different tissues among seven animals that had prostate (n=4) or liver (n=3) cancer.

for lactate and alanine are in the same range as pyruvate. We measured generally shorter T_1 values, which we attribute to undesired attenuation by the spin-echo refocusing pulses both for flowing spins as well as in the transition regions of the RF coil during the dynamic acquisition (21).

The Kpl and Kpa are markers of the tissue metabolic profile. Similarly to previous studies, a larger Kpl value was associated with cancerous tissue (*Figure 4*). In addition, Kpa variation was low in comparison to Kpl among all voxels. A significant difference was observed (P<0.001) between cancerous tissues and non-cancerous tissues.
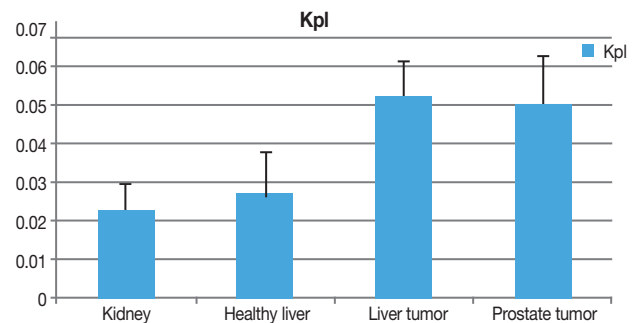
Figure 5 shows the correlation between Kpl and the lactate to pyruvate signal ratio in Eq. [4] is approximately linear, suggesting either could be used to measure metabolism.

Figures 6 and 7 show sample images of our total pyruvate, Pp, and urea, Pu, perfusion parameterizations. As it is clear and shown with an arrow in *Figure 6A*, the Kpl values in the cancerous tissues are high. Substantial variation of pyruvate

perfusion and urea perfusion can be observed for healthy and cancerous tissues.

Mapping of the kinetic and perfusion parameters allows for observation of spatial heterogeneity, as can be observed by varying Kpl values in *Figure 6A* across the tumor. In the
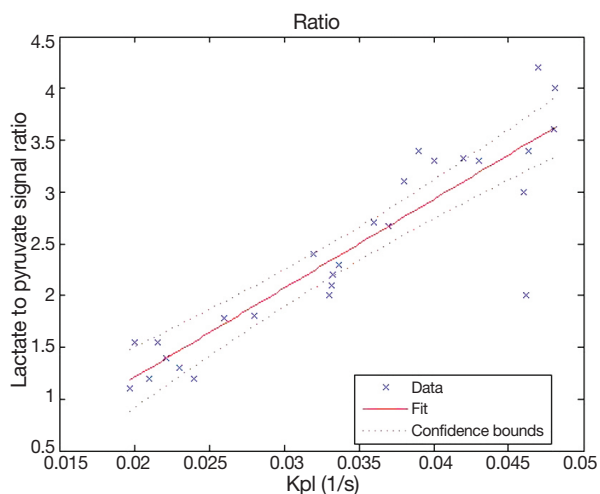

Figure 5 Correlation between Kpl and lactate to pyruvate signal across kidney, liver, and both tumor tissue types, which had a correlation coefficient of 0.95.

prostate tumor slice (*Figure 6A*) we can identify a lymph node with metastatic disease in the bottom left of the slice which has a very high Kpl, while low Kpl and low perfusion in parts of primary tumor are likely necrosis. The amount of pyruvate perfusion in *Figure 6F* in liver is very low. In *Figure 6G* high urea perfusion in the primary tumor can be observed and approximately correlates with Kpl. However, the lymph node metastasis had low pyruvate and urea perfusion but high Kpl.

The same metabolite parameter mapping for a mouse with liver cancer is shown in *Figure 7*. Kpl values in *Figure 7A-C* are significantly higher in the liver cancerous tissue (red arrow) with respect to the healthy part of liver (green arrow) and kidney. A small amount of pyruvate perfusion was observed in kidneys in *Figure 7F*) in comparison to the liver tumor while the urea perfusion as we expected is higher in kidneys (*Figure 7I*).

To compare our perfusion parameterizations across animals, we normalized P_p and P_u to the kidney values. In *Figure 8* the ratio of normalized total pyruvate perfusion over normalized urea perfusion (P_p:P_u) is shown. We observed this ratio was increased in both liver and prostate tumors. We believe this is due to increased uptake (and subsequent metabolic conversion) of pyruvate compared to
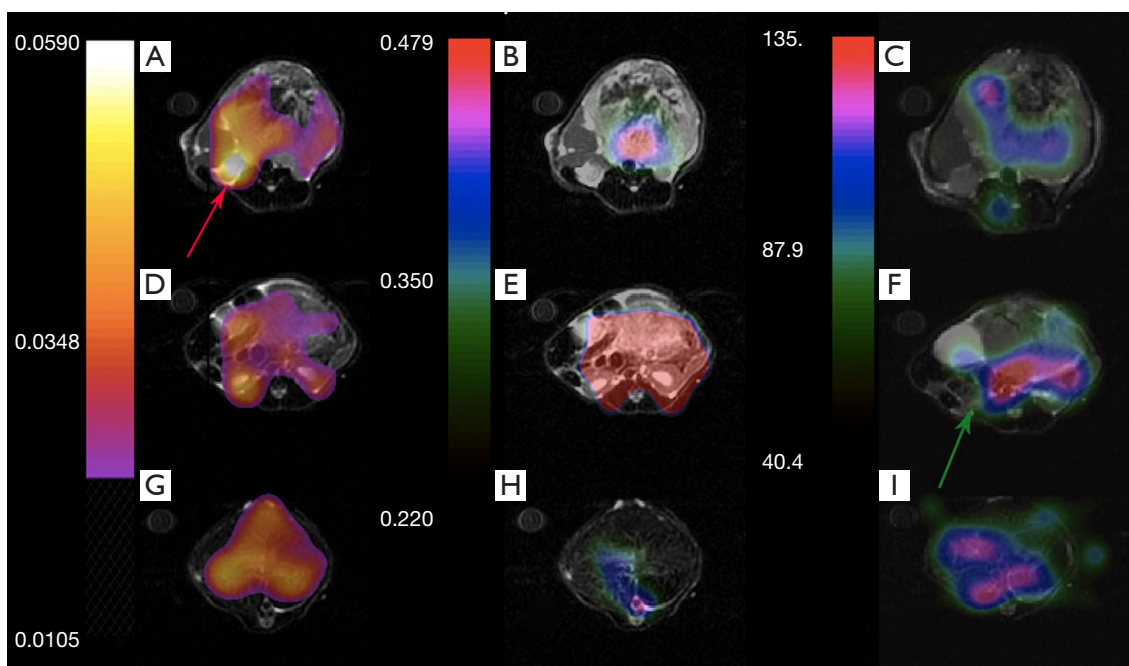

Figure 6 Mapping of Kpl (A-C), total pyruvate perfusion (D-F) and urea perfusion (G-I) in the same slices of prostate cancer, kidneys, and liver as *Figure 3*.
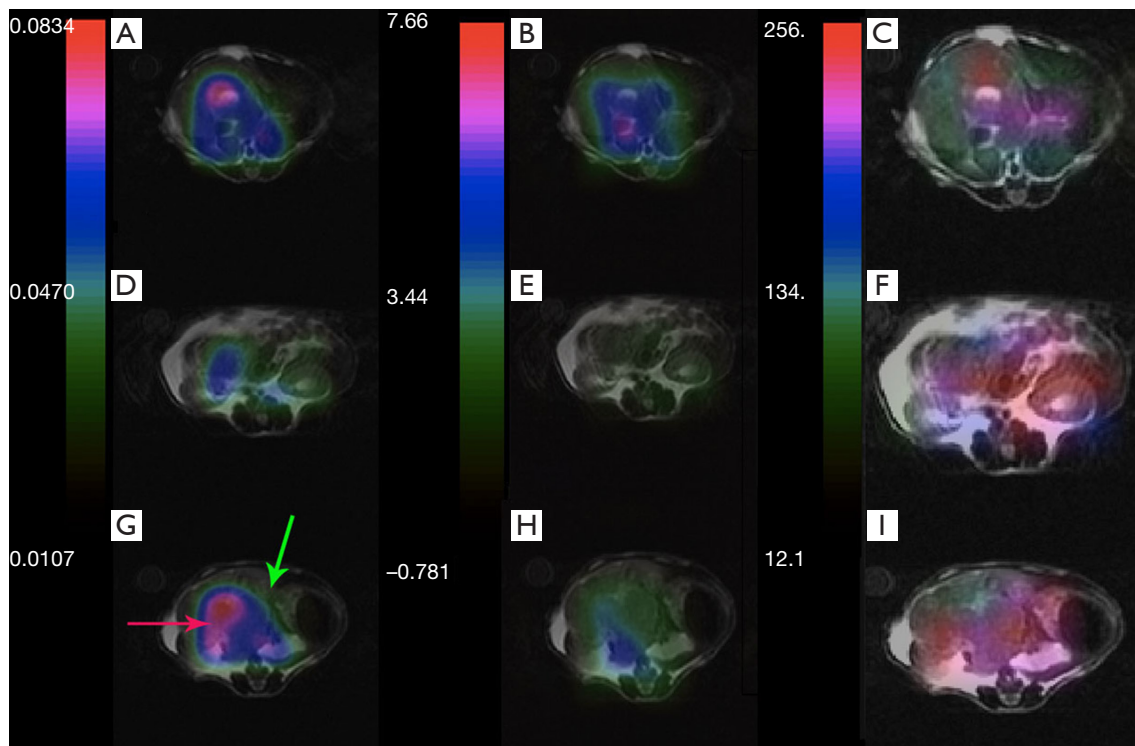
Figure 7 Mapping of Kpl (A-C), total pyruvate perfusion (D-F) and urea perfusion (G-I) in the same slices of liver cancer, kidneys, and both healthy and cancerous liver as *Figure 2*.
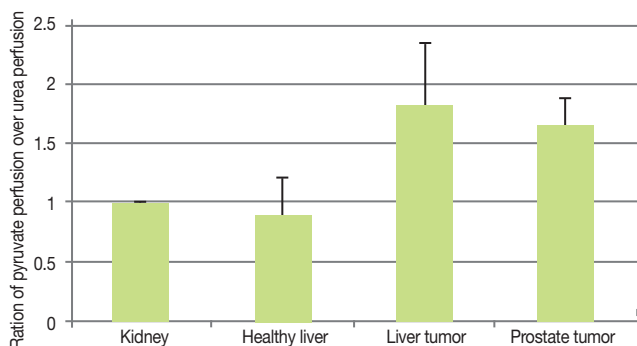

Figure 8 The total pyruvate perfusion to urea perfusion ratio across various tissues. This ratio was significantly different (P<0.001) between both tumor type and either healthy tissue. (All metabolites' perfusion were normalized to the perfusion values in the kidneys).

urea, which is primarily in the vasculature.

Discussion

We made two important assumptions in our kinetic model: (I) the backward reaction rates (KLP and KAP) were zero, an assumption that has been used extensively in hyperpolarized pyruvate modeling; (II) the T_1 relaxation rate was identical for pyruvate, lactate and alanine. We determined this was necessary based on a Monte Carlo analysis fitting of simulated data with SNR similar to our *in vivo* data. If the individual relaxation rates were not assumed to be equal, our simulations showed that the kinetic model fitting would be unreliable and not reproducible. This is a limitation of our model, as the metabolite relaxation rates are probably not equal.

The fit values for T_1s are actually effective T_1 values, and reflect both T_1 as well as losses due to flow and pulse sequence imperfections. Estimation of kinetic model parameters is challenging *in vivo* due physiologic effects (blood flow, respiratory/cardiac motion) and relatively low SNR in dynamic MRSI (22). Extracting the T_1 of the metabolites provides additional information to characterize cancerous versus healthy tissues. The range 20-45 (s) is reasonable for metabolites' T_1 values (*Table 1*). These are shorter than some previously measured values, which we attribute to undesired attenuation by the spin-echo refocusing pulses both for flowing spins as well as in the transition regions of the RF coil (21).

The kinetic modeling presented can easily be modified

www.amepc.org/qims   *Quant Imaging Med Surg* 2014;4(1):24-32

for data acquired with an arbitrary set of flip angles that can vary over time. This is done through a simple modification of Eq. [3], and enables the use of more efficient flip angle schemes (23).

We observed a strong correlation between Kpl and the total lactate to total pyruvate ratio, as others have also shown. The ratio is a simpler calculation and easier to implement than the kinetic modeling. However, we have determined through simulation that the total lactate to total pyruvate ratio is highly influenced by the delivery time of pyruvate, so care should be taken when using this ratio if variable vascular delivery rates are expected. Both the kinetic modeling and metabolite ratio are highly influenced by the actual RF flip angles, and precise B_1 calibration is important for quantitative measurements.

Measurement of urea perfusion can be a marker vascular delivery since urea primarily stays in the vasculature. Liver is a very vascular organ and the opened capillary shape of liver vasculature likely caused high urea perfusion in liver. The kidneys are highly vascularized and are also responsible for concentrating urea for removal in the urine. In tumors, the tissue request for blood is high but in a more uncontrolled way because of the abnormality of blood vasculature and circulation inside most tumors. Thus the urea perfusion in tumors is likely more sporadic and random. Urea cannot perfuse well in some parts of tumor particularly in suspected necrotic regions. On the other hand, some parts of tumor have more metabolic activity and, therefore, these parts need more blood and more vessels, and consequently should have more urea perfusion.

Our total pyruvate and urea perfusion parameterizations are different from conventional perfusion modeling, and were designed as a simple representation of the total amount of these compounds that are present in the tissue. In particular, the total pyruvate perfusion also includes any pyruvate or metabolic products that remain in the tissue, in addition to those present in the vasculature. The urea perfusion should primarily represent the vasculature delivery since it primarily stays in the vessels, while the total pyruvate perfusion can also be a marker for vascular delivery but also includes tissue uptake. We hypothesize that when the pyruvate perfusion is higher relative to urea perfusion it represents a higher amount of uptake of the pyruvate that is flowing into the tissue.

Conclusions

In this study we fit metabolite T_1 values, conversion rates,

Kpa, and Kpl, and measured novel pyruvate and urea perfusion parameterizations across cancerous and normal tissues from data acquired with a multiband RF excitation, compressed sensing dynamic MRSI pulse sequence. Our modeling allowed for use of arbitrary RF flip angles between metabolites, which in turn allows for efficient usage of the hyperpolarized magnetization. We observed a high correlation between our Kpl fits and the total lactate to pyruvate signal ratio, suggesting either could be used to characterize pyruvate-lactate metabolism. Through the novel pyruvate and urea perfusion parameterizations we were able to quantify the increased uptake of pyruvate in cancerous tissues, which correlated with increased metabolic conversion to lactate. These provided a more complete characterization of cancerous tissue metabolism and perfusion.

Acknowledgements

References

1. Carroll PR. Early stage prostate cancer--do we have a problem with over-detection, overtreatment or both? J Urol 2005;173:1061-2.
2. Kurhanewicz J, Vigneron DB, Brindle K, et al. Analysis of cancer metabolism by imaging hyperpolarized nuclei: prospects for translation to clinical research. Neoplasia 2011;13:81-97.
3. Golman K, Olsson LE, Axelsson O, et al. Molecular imaging using hyperpolarized 13C. Br J Radiol 2003;76 Spec No 2:S118-27.
4. Kaplan-Lefko PJ, Chen TM, Ittmann MM, et al. Pathobiology of autochthonous prostate cancer in a pre-clinical transgenic mouse model. Prostate 2003;55:219-37.
5. Ardenkjaer-Larsen JH, Fridlund B, Gram A, et al. Increase in signal-to-noise ratio of > 10,000 times in liquid-state NMR. Proc Natl Acad Sci U S A 2003;100:10158-63.
6. Golman K, Petersson JS. Metabolic imaging and other applications of hyperpolarized 13C1. Acad Radiol 2006;13:932-42.
7. Albers MJ, Bok R, Chen AP, et al. Hyperpolarized 13C lactate, pyruvate, and alanine: noninvasive biomarkers for prostate cancer detection and grading. Cancer Res 2008;68:8607-15.
8. Bahrami N, Rezatofighi SH, Adeli AM, et al. Boundary delineation for hepatic hemangioma in ultrasound images.

www.amepc.org/qims   *Quant Imaging Med Surg* 2014;4(1):24-32

Conf Proc IEEE Eng Med Biol Soc 2011;2011:7989-92.

9. Gingrich JR, Barrios RJ, Morton RA, et al. Metastatic prostate cancer in a transgenic mouse. Cancer Res 1996;56:4096-102.

10. Greenberg NM, DeMayo F, Finegold MJ, et al. Prostate cancer in a transgenic mouse. Proc Natl Acad Sci U S A 1995;92:3439-43.

11. Bernatowicz P, Kowalewski J, Szymanski S. Nuclear-spin relaxation in nonrigid molecules: discrete multisite local dynamics combined with anisotropic molecular reorientation. J Chem Phys 2006;124:024108.

12. Gillies RJ, Schornack PA, Secomb TW, et al. Causes and effects of heterogeneous perfusion in tumors. Neoplasia 1999;1:197-207.

13. Chen AP, Albers MJ, Cunningham CH, et al. Hyperpolarized C-13 spectroscopic imaging of the TRAMP mouse at 3T-initial experience. Magn Reson Med 2007;58:1099-106.

14. Vaupel P, Kallinowski F, Runkel S, et al. Blood flow and oxygen consumption rates of human gynecological tumors xenografted into rnu/rnu-rats. Strahlenther Onkol 1989;165:502.

15. Park I, Larson PE, Zierhut ML, et al. Hyperpolarized 13C magnetic resonance metabolic imaging: application to brain tumors. Neuro Oncol 2010;12:133-44.

16. Goga A, Yang D, Tward AD, et al. Inhibition of CDK1 as a potential therapy for tumors over-expressing MYC. Nat Med 2007;13:820-7.

17. Shachaf CM, Kopelman AM, Arvanitis C, et al. MYC inactivation uncovers pluripotent differentiation and tumour dormancy in hepatocellular cancer. Nature 2004;431:1112-7.

18. Puckeridge M, Pagès G, Kuchel PW. Simultaneous estimation of T_1 and the flip angle in hyperpolarized NMR experiments using acquisition at non-regular time intervals. J Magn Reson 2012;222:68-73.

19. von Morze C, Larson PE, Hu S, et al. Investigating tumor perfusion and metabolism using multiple hyperpolarized (13)C compounds: HP001, pyruvate and urea. Magn Reson Imaging 2012;30:305-11.

20. Chen AP, Kurhanewicz J, Bok R, et al. Feasibility of using hyperpolarized [1-13C]lactate as a substrate for in vivo metabolic 13C MRSI studies. Magn Reson Imaging 2008;26:721-6.

21. Josan S, Yen YF, Hurd R, et al. Application of double spin echo spiral chemical shift imaging to rapid metabolic mapping of hyperpolarized [1-^{13}C]-pyruvate. J Magn Reson 2011;209:332-6.

22. Bosman L, Madhu PK, Vega S, et al. Improvement of homonuclear dipolar decoupling sequences in solid-state nuclear magnetic resonance utilising radiofrequency imperfections. J Magn Reson 2004;169:39-48.

23. Xing Y, Reed GD, Pauly JM, et al. Optimal variable flip angle schemes for dynamic acquisition of exchanging hyperpolarized substrates. J Magn Reson 2013;234:75-81.